Physical properties of hexagonal BaPtAs with noncentrosymmetric SrPtSb-type and centrosymmetric YPtAs-type crystal structures: Effects of spin-orbit coupling

H. M. Tütüncü,[1,2] Ertuğrul Karaca,[2] H. Y. Uzunok,[1,2] and G. P. Srivastava[3]
[1]*Sakarya Üniversitesi, Fen-Edebiyat Fakültesi, Fizik Bölümü, 54187, Adapazarı, Turkey*
[2]*Sakarya Üniversitesi, BIMAYAM Biyomedikal, Manyetik ve Yarıiletken Malzemeler Araştırma Merkezi, 54187, Adapazarı, Turkey*
[3]*School of Physics, University of Exeter, Stocker Road, Exeter EX4 4QL, United Kingdom*

(Received 18 April 2019; revised manuscript received 14 June 2019; published 7 November 2019)

Recently, superconductivity in BaPtAs with the noncentrosymmetric SrPtSb and the centrosymmetric YPtAs-structure has been discovered. Its noncentrosymmetric and centrosymmetric structures make BaPtAs a charming compound for searching the effect of spin-orbit coupling (SOC) onto superconductors with broken and preserved spatial inversion symmetry. We have investigated the effect of SOC on the physical and electron-phonon interaction properties of these phases of BaPtAs by using the generalized gradient approximation of the density functional theory and the plane-wave pseudopotential method. The inclusion of SOC has moderate effect on the elastic and electronic properties, and on phonon frequencies for both phases of BaPtAs. However, SOC makes an opposite impact on their Eliashberg spectral function. For the noncentrosymmetric phase, this coupling decreases the strength of dominant peaks of Eliashberg spectral function, reducing the values of average electron-phonon coupling and superconducting transition temperature. The scenario is exactly opposite for the centrosymmetric phase. For both phases, the hybridized Pt-As vibrations play a strongly significant role in determining their electron-phonon interaction properties since their electronic states have the dominant contribution near the Fermi level. The superconducting temperature is estimated to be 2.87 K for the SrPtSb phase and 2.38 K for the YPtAs phase. These values compare well with the reported measured values of 2.8 K and 2.1–3.0 K, respectively.

DOI: 10.1103/PhysRevB.100.174507

I. INTRODUCTION

In recent years, noncentrosymmetric superconductors (NCSs) have drawn a great deal of attention [1–10]. An absence of inversion symmetry causes internal electric field gradients and therefore produces an antisymmetric spin-orbit coupling (ASOC), which successively leads to a splitting of the energy bands and Fermi surface. Moreover, ASOC permits mixing of the spin-singlet and spin-triplet Cooper pairing states [1,2,6,10]. In 2004, a heavy fermion superconductor, $CePtSi_3$, without inversion symmetry, was reported [2], in which there is coexistence of superconductivity (transition temperature $T_c = 0.75$) and antiferromagnetic (transition temperature $T_N = 2.2$ K). There are a number of other examples of NCS including, for example, $CeRhSi_3$ [3], $CeIrSi_3$ [4], and $CeCoGe_3$ [5]. All these NCSs include the Ce element and display unusual magnetism because of the $4f$ electrons. Due to magnetic order and heavy fermion behavior, it is very difficult to investigate the effects of ASOC and inversion symmetry breaking on superconductivity of these Ce-based NCSs. In 2004, Togano and co-workers [11] reported the existence of superconductivity around 8 K in a metal-rich boride Li_2Pd_3B compound with cubic noncentrosymmetric structure. Following this discovery, its isostructural compound Li_2Pt_3B was reported to exhibit superconductivity at around 2 K [12,13]. Resistivity measurements displayed good metallic behavior in both these NCSs, while a magnetization experiment depicted no magnetic ordering in either compound [11–13]. Low-temperature specific-heat and neutron-diffraction studies [13] on these NCSs suggested that Li_2Pt_3B is a weakly coupled BCS-type superconductor while Li_2Pd_3B is an intermediately coupled BCS-type superconductor. In 2009, muon spin relaxation experiments [14] on the noncentrosymmetric intermetallic superconductor $LaNiC_2$ were conducted. An examination of the possible pairing symmetries confirmed the existence of four triplet states in this noncentrosymmetric superconductor [14]. Superconductivity at 3.3 K has also been observed in the noncentrosymmetric Ru_7B_3 [15]. This experimental study suggests that Ru_7B_3 belongs to a single band superconductor with an energy gap of 0.5 meV and can be classified as a type-II superconductor with weak electron-phonon coupling. Specific heat and electrical resistivity measurements [16] suggest $BaPtSi_3$ as another noncentrosymmetric superconductor with $T_c = 2.25$ K. All experimental parameters and examinations [16] signal a BCS-like superconductivity for $BaPtSi_3$, which is based on spin-singlet pairing with a fully gapped density of states at the Fermi level.

In addition to $BaPtSi_3$, several f-electron-free $BaNiSn_3$-type NCS have been discovered such as $LaRhSi_3$ [17], $CaPtSi_3$ [18], $CaIrSi_3$ [18], $LaPtSi_3$ [19], $LaPdSi_3$ [19], $LaIrSi_3$ [20], and $SrAuSi_3$ [21]. They do not exhibit strong electronic correlations, and superconductivity occurs at ambient pressure with conventional BCS character. In 2010, from resistivity, magnetic susceptibility, and specific-heat measurements [22], Mo_3Al_2C crystallizing in the noncentrosymmetric cubic β-manganese structure was categorized as a type-II superconductor with a transition temperature near 9.2 K. In 2014, Singh and co-workers [23] analyzed the

superconducting state of the noncentrosymmetric compound Re_6Zr using magnetization, heat capacity, and muon-spin relaxation or rotation (μSR) measurements. This noncentrosymmetric compound exhibits superconductivity at 6.75 K. The existence of spontaneous fields below T_c supply credible evidence for time-reversal symmetry breaking in this compound and an unconventional pairing mechanism. In 2016, Rh_2Mo_3N, with a noncentrosymmetric β-manganese structure, was reported to display superconductivity at around 4.3 K [24]. Electrical transport, specific heat, and magnetic measurements [24] revealed that this compound acts as a typical BCS type-II superconductor. Recently, Kudo and coworkers [25] have reported the synthesis and discovery of a new noncentrosymmetric superconductor BaPtSb. Electrical resistivity and specific-heat measurements signal that BaPtSb becomes superconducting at 1.64 K.

The report of several f-electron-free NCS has triggered theoretical studies on them in order to investigate the effect of the lack of inversion symmetry on superconductivity. The full-potential nonorthogonal local-orbital minimum-basis method (FPLO) [26] has been used to study electronic properties of NCS Li_2Pt_3B and Li_2Pd_3B. This theoretical work [26] indicates that the impact on the electronic band structure of spin-orbit coupling (SOC) plus the absence of inversion is outstanding, and is much larger in the Pt compound due its heavier mass than that of Pd. First-principles calculations of the electronic structure, phonons, and the electron-phonon coupling for $LaNiC_2$ have been carried out, while the thermodynamic properties of the superconducting state have been obtained numerically by solving the Eliashberg equations [27]. The results of this theoretical study [27] suggest that this noncentrosymmetric compound displays non-BCS superconducting properties, but with the electron-phonon coupling being the most likely the pairing mechanism. The electronic properties of noncentrosymmetric superconductor Ru_7B_3 have been investigated by using the full potential linear muffin-tin orbital [15]. Ruthenium $4d$ states dominates the electronic structure of this noncentrosymmetric superconductor while the contribution of boron $2p$ orbital is little. The electronic and vibrational properties of $BaPtSi_3$ have been analyzed by employing the density functional theory within the local density approximation [16]. In agreement with experimental results [16], this theoretical study [16] supports that the inclusion of SOC has little influence on the electronic bands near the Fermi level, and hence, superconductivity in $BaPtSi_3$ appears to be an almost untainted BCS state. The full-potential linearized augmented plane wave calculations [28] have been carried out to calculate the electronic structures of NCS $CaIrSi_3$ and $CaPtSi_3$. The results of this study have stated that transitional metal's d states and silicon's p states dominate the electronic states near the Fermi level. Following this theoretical work, full relativistic local-density approximation method [29] have been carried out to examine the electronic properties of NCS $CaIrSi_3$ and $CaPtSi_3$. The results of this theoretical study indicate that the inclusion of SOC makes only small effect on the electronic band structures of these NCSs near the Fermi level. Full-potential local-orbital (FPLO) calculations [30] have been conducted to view the electronic properties of $LaPdSi_3$. According to this theoretical work, the effect of ASOC on the electronic band structure of $LaPdSi_3$ is rather small. Recently, the linear response approach and the Migdal-Eliashbergh approach [31–34] have been combined to probe electron-phonon interaction properties of several $BaNiSn_3$-type NCS such as $SrAuSi_3$, $CaIrSi_3$, $LaIrSi_3$, $LaPdSi_3$, $LaRhSi_3$, and $LaPtSi_3$. The results of these theoretical studies [31–34] reveal that the impact of SOC on the electron-phonon interaction in these NCSs is little due to the weak effect of this coupling on their electronic band structures near the Fermi level. Furthermore, first-principles pseudopotential calculations [35] have been carried out to investigate the effect of SOC on superconductivity in the noncentrosymmetric BaPtSb superconductor. This theoretical work [35] reveals that the value of average electron-phonon coupling parameter of this noncentrosymmetric superconductor is increased from 0.62 to 0.63 with the consideration of SOC. This increase in the value of the average electron-phonon coupling parameter increases the value of its superconducting temperature from 1.46 to 1.54 K.

Very recently, the intermetallic compound BaPtAs has been reported to depict polymorhism [36]. Although formerly this compound was reported to adopt the cubic LaIrSi-type crystal structure, recent single-crystal x-ray diffraction measurements [36] reveal that it also exists in the hexagonal SrPtSb-type crystal structure as well as in the hexagonal YPtAs-type crystal structure. Furthermore, magnetization, electrical resistivity, and specific heat measurements [36] conclude that the SrPtSb- and YPtAs-type BaPtAs exhibit superconductivity at 2.8 and 2.1–3.0 K, respectively, while its cubic LaIrSi-type structure becomes superconductor only below 0.1 K. The hexagonal SrPtSb- and YPtAs-type crystal structures of BaPtAs are illustrated in Fig. 1. The SrPtSb phase of BaPtAs can be considered as a ternary rowed derivative of the AlB_2 type structure: The Pt and As atoms alternately assume the B site, building a PtAs rowed network. The honeycomb layers are accumulated along the z axis in such way that a Pt and As atom exists above each Pt and As atom, respectively, constituting a -Pt(As)-PtAs- stowing row, as displayed in Fig. 1(a). As a consequence, the SrPtSb phase of BaPtAs does not contain a center of inversion. Therefore this phase of BaPtAs can be classified as a noncentrosymmetic superconductor. The YPtAs phase of BaPtAs is composed of alternating accumulated Ba triangular, rowed, and weakly puckered PtAs honeycomb networks, as depicted in Fig. 1(b). This phase of BaPtAs can be categorized as the four-layer derivative of the AlB_2-type structure. The PtAs rowed honeycomb layers are accumulated along the z axis in such way that constitutes a -As(Pt)-As(Pt)-Pt(As)-Pt(As)- stowing row [also see Fig. 1(b)]. As a consequence, this phase of BaPtAs contains a center of inversion. Therefore the YPtAs phase of BaPtAs can be classified as a centrosymmetric superconductor. Consequently, the SrPtSb and YPtAs phases of BaPtAs ensure an excellent platform for probing the impact of spin-orbit coupling onto superconductors with broken and conserved spatial inversion symmetry.

In this work, we have purposed to investigate the effect of SOC on the electronic, elastic, mechanical, phonon and electron-phonon interaction properties of the SrPtSb- and YPtAs-type BaPtAs. *Ab initio* pseudopotential electronic structure calculations [37,38] within the generalized gradient approximation (GGA) have been made. The impact of SOC on

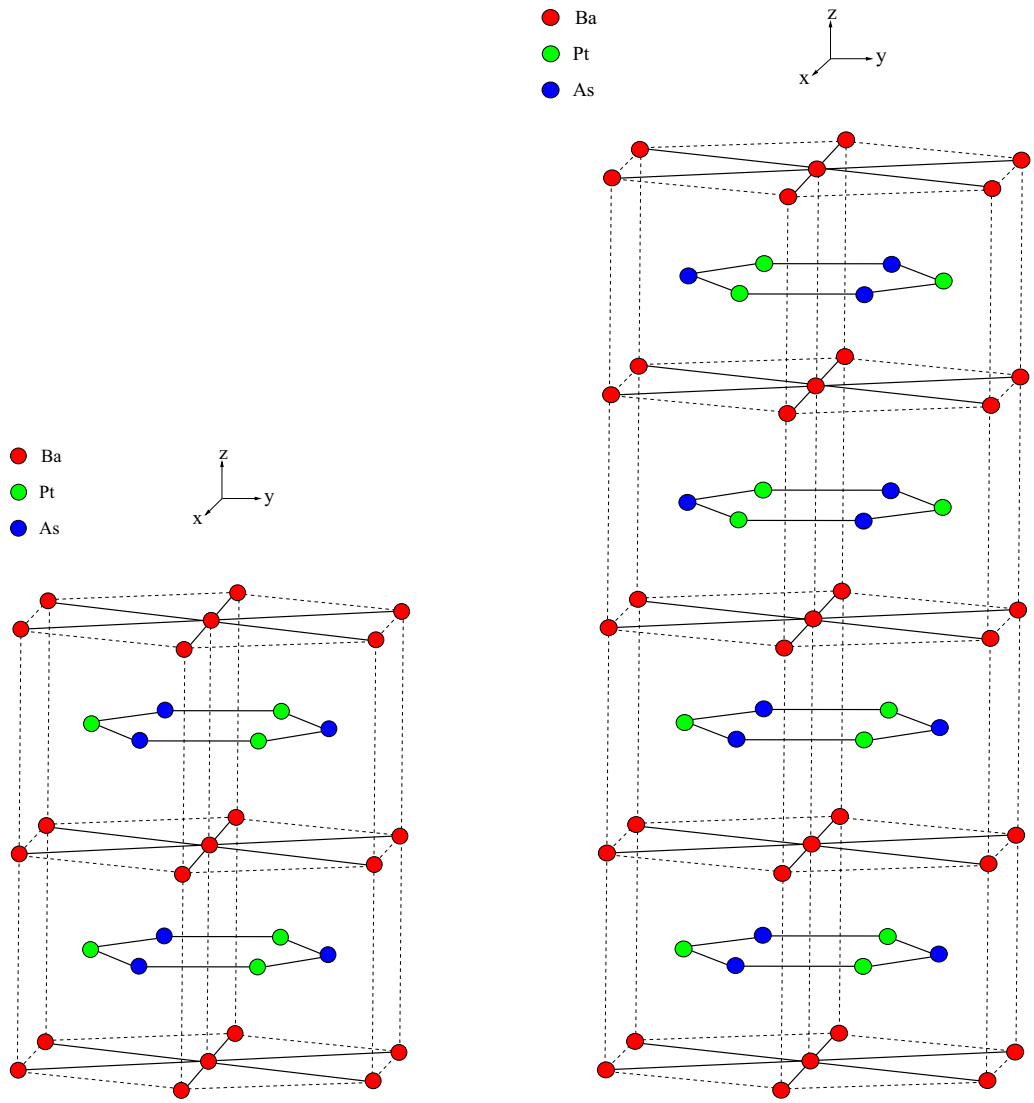

(a) SrPtSb Phase (b) YPtAs Phase

FIG. 1. (a) The hexagonal SrPtSb-type crystal structure of BaPtAs. This phase of BaPtAs does not possess a center of inversion, making it a noncentrosymmetric superconductor. (b) The hexagonal YPtAs-type crystal structure of BaPtAs. This phase of BaPtAs has a center of inversion symmetry, and thus can be categorized as a centrosymmetric superconductor.

the electronic structures for both phases of BaPtAs is analyzed and discussed in detail. Second order elastic constants for both phases of BaPtAs have been determined by using the strain-stress method [39] while the isotropic bulk modulus (B_{VRH}), the isotropic shear modulus (G_{VRH}), Poisson's ratio (ν), and Young's modulus (E) have been obtained by the help of the Voigt-Reuss-Hill (VRH) scheme [40–42]. Phonon calculations for both phases of BaPtAs have been made by using a linear response approach [37,38]. The Eliashberg spectral function has been determined by combining the linear response method [37,38] and the Migdal-Eliashberg approach [43,44]. The average electron-phonon coupling parameter and the logarithmic average of phonon frequency for both phases have been evaluated by integrating their Eliashberg spectral functions. These physical quantities are used to calculate the superconducting transition temperatures for both phases of BaPtAs by the help of the modified Allen-Dynes formula [45]. Finally, the effect of spin-orbit coupling on the superconducting parameters of both phases is presented and disputed in detail.

II. METHOD

The quantum mechanical calculations have been executed by using the QUANTUM ESPRESSO *ab initio* simulation package [37,38], in which the plane-wave pseudopotential method is applied. For calculations with SOC, the ion-electron interaction was modeled by using full relativistic ultrasoft pseudopotentials [46]. Non-SOC calculations were made by using scalar-relativistic ultrasoft pseudopotentials [46]. The impact of exchange-correlation was treated within the GGA of Perdew-Burke-Ernzerhof (PBE) scheme [47]. The plane-wave

basis cutoff was taken as 60 Ry for all realized calculations. Both phases of BaPtAs were fully relaxed by applying the Broyden-Fletcher-Goldfrab-Shanno optimized method [48]. The solution of Kohn-Sham equations [49] was sought by using an iterative conjugate gradient scheme, applying a set of Monkorst-Pack special $\boldsymbol{k}$ points [50]. The Brillouin zone integration for the computation of total energies for both phases of BaPtAs was carried out by employing the (8×8×8)-$\boldsymbol{k}$ mesh. On the other hand, electronic calculations were performed by using a denser (24 × 24 × 24)-$\boldsymbol{k}$ mesh for the SrPtSb phase of BaPtAs and a denser (20 × 20 × 20)-$\boldsymbol{k}$ mesh for the YPtAs phase of BaPtAs.

Phonon calculations were performed within the harmonic approximation by making use of the linear response approach as implemented in the Quantum-Espresso *ab initio* simulation package [37,38]. The Brillouin zone integration for the phonon calculation of SrPtSb-type BaPtAs was made by using a (8×8 × 8) grid while the same calculation for the YPtAs phase of BaPtAs was realized by using a (4 × 4 × 4) grid. It is worth to mention that phonon frequencies are converged to within 0.01 THz in our calculations. For the both phases of BaPtAs, we have directly computed twelve dynamical matrices for a (4 × 4 × 4)-$\boldsymbol{k}$ mesh. Then, they were Fourier-transformed to real space and thus the force constants obtained, which are used to get phonon frequencies for any $\boldsymbol{q}$ points. The linear-response approach [37,38] and the Migdal-Eliashberg theory [43,44] were combined to compute the electron-phonon interaction matrices for both phases of BaPtAs. More details about the electron-phonon interaction are provided in our previous calculations [51]. However, it is worth to mention that the Fermi surface sampling for the estimating of the electron-phonon interaction matrix elements were conducted using a denser (24 × 24 × 24)-$\boldsymbol{k}$ mesh for the SrPtSb phase of BaPtAs and a denser (20 × 20 × 20)-$\boldsymbol{k}$ mesh for the YPtAs phase of BaPtAs.

III. RESULTS

A. Structural and electronic properties

As can be seen from Fig. 1(a), the first phase of BaPtAs crystallizes in the hexagonal noncentrosymmetric SrPtSb-type crystal structure with the space group $P\bar{6}m2$, which includes one formula unit in the primitive unit cell with Wyckoff positions of atoms at Ba (1a) (0, 0, 0), Pt (1d) (1/3, 2/3, 1/2), and As(1f) (2/3, 1/3, 1/2). Therefore two lattice parameters (a and c) are enough to define the SrPtSb phase of BaPtAs. Figure 1(a) obviously illustrates that this phase of BaPtAs is a ternary ordered variant of the hexagonal AlB_2-type structure. As can be seen from Fig. 1(b), the second phase of BaPtAs adopts the hexagonal centrosymmetric YPtAs-type crystal structure with space group $P6_3/mmc$, and four formula units per primitive cell. The atomic configuration includes two Ba atoms at the (2a) (0, 0, 0) position, two Ba atoms at the 2(b) (0, 0, 1/4) position, four Pt atoms at the 4(f)(1/3, 2/3, z_{Pt}) position, and four As atoms at the 4(f)(1/3, 2/3, z_{As}) position. Thus this phase of BaPtAs is formed by two lattice parameters (a and c) and two inner parameters (z_{Pt} and z_{As}). This phase of BaPtAs can be classified as the four-layer superstructure derivative of the hexagonal AlB_2-type structure.

To start with, we conducted the structural optimization calculations for both phases of BaPtAs under the minimum conditions of the total energy and the forces acting on the atoms. Then, the values of bulk modulus (B) and its pressure derivative (B') for both phases of BaPtAs have been attained by minimizing the crystal total energy for different values of the crystal volume by means of the Murnaghan equation of state [52]. Table I presents the calculated values of a, c, B, and B' for the both phases of BaPtAs, and the calculated values of z_{Pt} and z_{As} for the YPtAs phase of BaPtAs along with experimental results [36] for the values of lattice parameters and inner coordinates. The values of a and c for both phases accord very well with their measured values [36] while the calculated values of z_{Pt} and z_{As} for the YPtAs phase harmonize excellently with their experimental values [36]. In particular, the maximum deviation is observed for the c lattice constant value of YPtAs phase within around 2%. Unfortunately, no experimental data and previous theoretical results are available for the values of B and B' for both phases.

The absence of inversion symmetry in a crystal generates an electric field gradient along the symmetry breaking direction that gives rise to a Rashba-type ASOC [53,54]. Due to this ASOC, the Fermi sheets are split into two different surfaces with oppositely spinned electrons. Because of this splitting, the electrons could create a Cooper pair without phonon exchange, which leads an unconventional superconductivity [53,54]. For this reason, the vertical splitting of the electronic bands around the Fermi energy level and their Fermi surface sheets have to be examined. Hence, we have

TABLE I. The calculated values of the lattice parameters (a and c), equilibrium volume, bulk modulus (B), and its pressure derivative (B') for hexagonal BaPtAs with SrPtSb and YPtAs crystal structures. The internal parameters (z_{Pt} and z_{As}) for the YPtAs phase of BaPtAs are also presented. Experimental values of the lattice parameters and internal parameters are also included for comparison.

	SrPtSb phase						
	a (Å)	c (Å)	V (Å^3)	B (GPa)	B'		
This work with SOC	4.3703	4.8445	80.1312	64.10	4.36		
Experimental [36]	4.3084	4.7615	76.5432				
	YPtAs phase						
	a (Å)	c (Å)	V (Å^3)	z_{Pt}	z_{As}	B (GPa)	B'
This work with SOC	4.3592	19.5161	321.1716	0.12333	0.62693	64.00	4.13
Experimental [36]	4.3244	19.1018	309.3546	0.12437	0.62640		

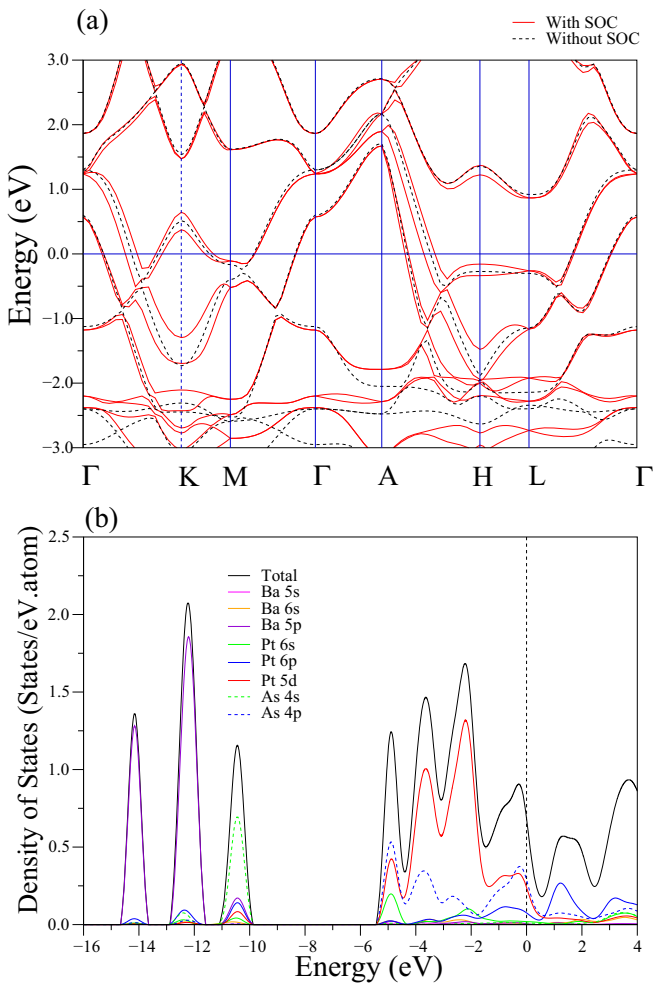

FIG. 2. (a) The calculated electronic band structure for the SrPtSb-type structure of BaPtAs with and without SOC along the high-symmetry directions in the first Brillouin zone of hexagonal lattice. (b) The calculated total and partial electronic density of states for the SrPtSb-type structure of BaPtAs with SOC included.

calculated the electronic band structure of SrPtSb-type BaPtAs both in a scalar relativistic approximation, ignoring SOC and fully relativistically, considering SOC in a self-consistent manner. Both results for the SrPtSb phase of BaPtAs are presented together in Fig. 2(a) along several high-symmetry lines of hexagonal Brillouin zone. According to this figure, the influence of SOC on the electronic structure of SrPtSb-type BaPtAs is twofold. First, some of the degeneracies at the H symmetry point are removed when SOC is included. For example, the splitting of electronic bands due to SOC amounts to 0.18 and 0.15 eV below and above the Fermi level, respectively. Secondly, the absence of inversion symmetry in the SrPtSb phase of BaPtAs might result in ASOC which is liable for removing the twofold degeneracy of electronic bands in the high-symmetry directions, except the M-Γ and Γ-A symmetry directions. In particular, the splitting of electronic bands arising from ASOC at the K point amounts to 0.40 and 0.27 eV below and above the Fermi level. According to Fig. 2(a), the twofold degeneracy of electronic bands still subsists along the M-Γ ([010]) and Γ-A ([001]) symmetry lines since the ASOC effect materializes only perpendicular to directions which break inversion symmetry. The inversion symmetry in the SrPtSb-type BaPtAs is broken by the arrangement of atoms along [010] and [001] directions [see Fig. 1(a)]. A similar observation has been made for the noncentrosymmetric BaPtSb superconductor [33]. This is not surprising because both centrosymmeric superconductors are isostuctural and isoelectronic to each other.

We have calculated the total and partial electronic density of states for the SrPtSb phase of BaPtAs in order to find out the atomic orbital origin of its electronic structure and our results with SOC are presented in Fig. 2(b). The total DOS displays several gripping features which can be well understood by analyzing the partial DOS. The first two peaks at around −14.2 and −12.24 eV consist mainly of Ba 5p states while the third peak at −10.4 eV arises from the s state of As atom. For the SrPtSb phase of BaPtAs, the main valence band region extends from −5.4 eV to the Fermi level. This region is mainly dominated by Pt and As electronic states while the contribution of Ba electronic states is negligible and featureless. This observation is anticipated since Ba atom is almost in the charge state close to Ba^{+2}. This reveals that Ba atom is bonded with the remaining atoms by ionic interactions. In particular, there are four peaks with energies of −4.9, −3.6, −2.2, and −0.13 eV in the main valence band region. The peak at −4.9 eV is mainly derived from the hybridization of As 4p and Pt 5s states with a lesser contribution from Pt 6s state. Therefore this peak is the first evidence of covalent interaction between Pt and As atoms. The next two peaks are mainly formed by Pt 5d states while the last peak feature is again due to the hybridization of As 4p and Pt 5d states. Therefore this peak feature is the second evidence of covalent interaction between Pt and As atoms while the finite DOS at the Fermi level confirms the metallic nature of SrPtSb-type BaPtAs. As a consequence, the bonding in the SrPtSb-type BaPtAs involves a combination of metallic, covalent, and ionic character. Since electrons close to the Fermi level govern the superconducting properties of materials according to the well-known BCS theory, the density of states at the Fermi level [$N(E_F)$] must be presented and discussed in detail. For the SrPtSb-type BaPtAs, the value of $N(E_F)$ amounts to 0.641 states/eV per atom, which is lowered to 0.612 states/eV per atom without the consideration of SOC. Now, we have to analyze the contributions of electronic orbitals to the value of $N(E_F)$. The contributions of Ba, Pt, and As to $N(E_F)$ are about 2%, 52%, and 46%, respectively. Most especially, Pt 5d and As 4p orbitals alone contribute, respectively, 38% and 44% to the value of $N(E_F)$. Now, we can conclude that Pt 5d and As 4p orbitals play the main role in the formation of the superconducting state for the SrPtSb-type BaPtAs.

The electronic structure and electronic total and partial DOS of YPtAs-type BaPtAs compound are presented in Fig. 3. The electronic band structure calculations are done with and without SOC as presented in Fig. 3(a). In contrast to the SrPtSb-type structure, the YPtAs-type BaPtAs has conserved its centrosymmetry along all the directions within its crystal structure. Hence, while the fourfold degeneracies split into twofold degeneracies at the high-symmetry points, the twofold degeneracies along the high-symmetry points conserve their degeneracies. This splitting can be seen especially

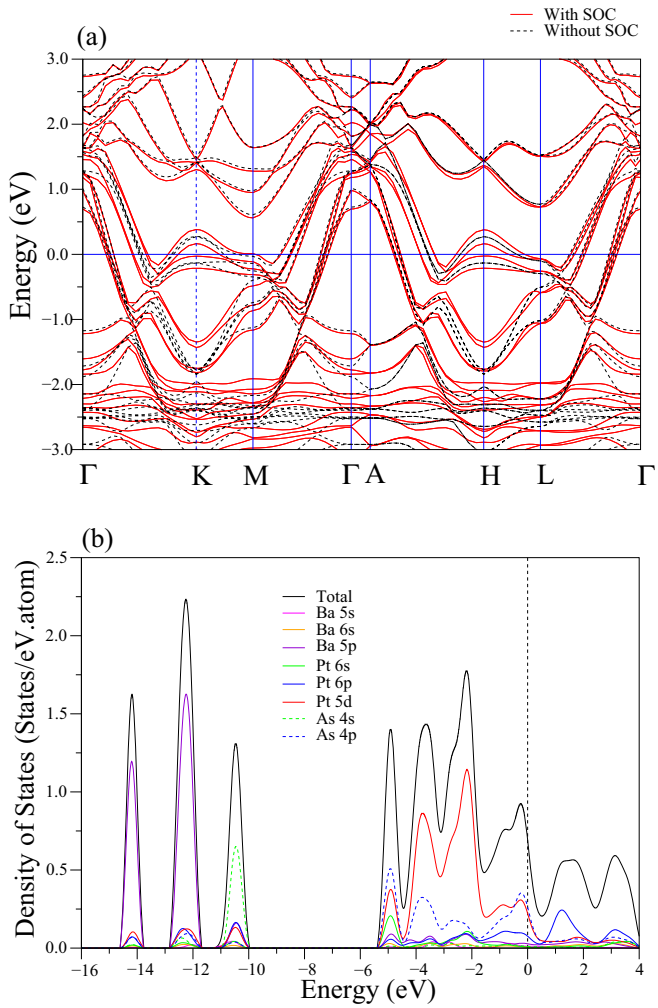

FIG. 3. (a) The calculated electronic band structure for the YPtAs-type structure of BaPtAs with and without SOC along the high-symmetry directions in the first Brillouin zone of hexagonal lattice. (b) The calculated total and partial electronic density of states for the YPtAs-type structure of BaPtAs with SOC included.

at the K and H symmetry points near the Fermi level. At K high-symmetry point, the fourfold degeneracy at 0.25 eV just above the Fermi level is split into twofold degeneracies that settle at 0.16 and 0.37 eV with an energy splitting of around 0.21 eV. Also just below the Fermi level at -1.77 eV, the fourfold degeneracy is split into twofold degeneracies that settled at -0.03 and -0.22 eV. Similar observations are made for the energy bands above and below the Fermi level at the H symmetry point. As the highest splitting energy due to SOC is calculated 0.25 eV, we could say that the effect of SOC on the electronic characteristic for this compound is quite low. Even though these splittings are not large enough to consider SOC, one of the split bands gets closer to the Fermi level which could cause an increase in the $N(E_F)$ value for this compound.

A comparison of results presented in Figs. 2(b) and 3(b) indicates that the electronic DOS of the YPtAs-type BaPtAs compound has features similar to that for the SrPtSb-type one, except for some minor differences. The contribution that is coming from Pt $5d$, Pt $6p$, and As $4p$ states to the first peak around -14.0 eV is larger than the contributions coming from the corresponding states to the first peak in the SrPtSb-type BaPtAs. A similar observation has been made for the second peak: the dominant Ba $5p$ state in this peak is waned a bit and the other states' contributions are increased, as can be seen in Fig. 3(b) when compared with the Fig. 2(b). Also the valence band is mainly constituted by the As $4p$ and Pt $5d$ states with lesser contributions from remaining Pt and As electronic states. Different from the SrPtSb-type one, the valence region of YPtAs-type BaPtAs has relatively more contribution coming from the remaining Ba $5p$, Pt $6p$, and Ba $6s$ states. The $N(E_F)$ features show that the Fermi level characteristics remain the same even though the crystal structure has changed. The calculated $N(E_F)$ value for YPtAs-type BaPtSb is 0.627 states/eV per atom with SOC, and 0.603 states/eV per atom without SOC. As it is predicted before, the $N(E_F)$ value with SOC considered is larger than the one without SOC. The contributions of Ba, Pt and As to $N(E_F)$ are about 7%, 53%, and 40%, respectively. Compared to the SrPtSb-type BaPtAs, the $N(E_F)$ of YPtAs-type BaPtAs has relatively larger contribution coming from Ba atom states. Particularly, percentage contributions to the value of $N(E_F)$ from Pt $5d$ and As $4p$ orbitals are calculated as 32% and 38%, respectively. We can conclude that the Cooper pairs in both phases are mainly constituted by the electrons from Pt $5d$ and As $4p$ orbitals.

The calculated Fermi surfaces of the SrPtSb-type and YPtAs-type BaPtAs with and without SOC are presented in Fig. 4 together. In SrPtSb-type BaPtAs two bands cross the Fermi level when the SOC is not considered. These bands extend from 1.61 to 1.71 eV and 0.55 to 2.17 eV. Along the Γ-A direction, the formation of the Fermi sheets makes the Fermi surface look like hollow tubes. The electronic bands constitute a closed Fermi surface around the K symmetry point. When the SOC is included, both Fermi sheets are split into two different surfaces because of the ASOC, as there is no inversion symmetry for the SrPtSb-type compound. Especially, the difference in the Fermi surfaces because of the horizontal splittings along the Γ-K, K-M, and A-H points can be clearly seen at the right panel of Fig. 4. As the YPtAs-type BaPtAs compound has an inversion symmetry, there is no sign of ASOC effect detected in the electronic band structure. When the SOC is included, the fourfold degenerated bands are split into twofold bands as can be seen from the Fig. 3(a). This split effect can be seen in the Fermi surfaces with SOC at bottom right panel in Fig. 4. As the inversion symmetry is conserved in this compound, the horizontal splitting at the Fermi level is negligible. There are a total of eight bands crossing the Fermi level within the range of -1.80 and 1.71 eV. Six of these bands from hollow cylindrical surfaces around the Γ- A direction. The other two bands form similar shape around the K point.

B. Elastic and mechanical properties

Elastic properties of superconductors must be investigated since they are associated with several fundamental properties such as the equation of state and phonon spectrum. Furthermore, they are connected to the thermodynamic properties such as specific heat, thermal expansion, Debye temperature,

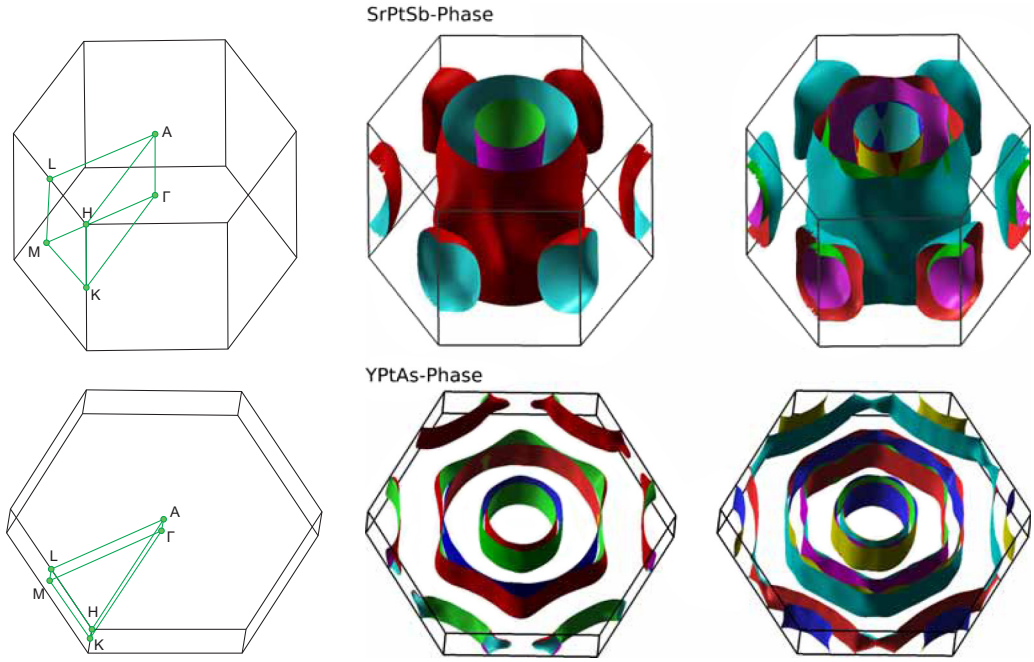

FIG. 4. Brillouin zone of hexagonal lattice (on the right), and the calculated 3D Fermi surface sheets with SOC (in the middle) and without SOC (on the left) of the SrPtSb-type and YPtAs-type structures of BaPtAs.

and melting point. For a hexagonal system, there are five linearly independent single-crystal elastic constants, namely, C_{11}, C_{12}, C_{13}, C_{33}, and C_{44}. The sixth one C_{66} equals to $\frac{1}{2}(C_{11} - C_{12})$. In this work, elastic constants calculations have been conducted using the effective stress-strain approach which appears to be the most widely used one in the literature [39]. The calculated full set of elastic constants for both phases of BaPtAs is presented in Table II. Unfortunately, there are no experimental data and previous theoretical results for comparison. Therefore future experimental and theoretical studies will testify our elastic constants results. As it is expected, the calculated elastic constants of both phases are very close to each other. Table II demonstrates that the inclusion of SOC makes a moderate impact on the values of elastic constants for both phases, with the maximum deviation of 9% for the C_{66} value of SrPtSb phase. The requirement of mechanical stability in hexagonal systems gives rise to the following restrictions on their single crystal elastic constants:

$$C_{44} > 0; \quad C_{11} > |C_{12}|; \text{ and } (C_{11} + 2C_{12})C_{33} > 2C_{13}.$$

Explicitly, from the calculated values of elastic constants in Table II, the above restrictions are all satisfied for both phases, revealing their mechanical stability at zero pressure. Furthermore, for both phases, C_{11} and C_{33} have larger values than remaining elastic constants which reveals that they are significant incompressible under uniaxial stress along x or z axis.

Using our calculated single-crystal elastic constants, we are able to derive the bulk modulus B_{VRH}, shear modulus G_{VRH}, Poisson's ratio (ν), and Young's modulus (E) for both phases of BaPtAs by the help of Voigt-Reuss-Hill (VRH) average scheme [40–42]. In the Reuss scheme [41], a uniform stress is supposed throughout the polycrystalline material, while the Voigt scheme [40] assumes that the strain throughout the polycrystalline material is uniform. Therefore Voigt and Reuss moduli exhibit the upper and lower bounds for true polycrystalline moduli, respectively. The Hill approximation [42], as an average of the two bounds, provides the best estimate for mechanical properties. The calculated values of B_{VRH}, G_{VRH}, E, B_H/G_H and ν for both phases are summarized in Table III. Unluckily, we could not come across any experimental data or previous theoretical results in the literature. However, the calculated values of B_H for both phases are close to their corresponding values determined from total energy calculations (see Tables I and III), suggesting the quality of our GGA results. The ratio of bulk modulus to shear modulus (B_H/G_H) is proposed as a criterion to differentiate between ductile and brittle characters of a compound. According to the empirical formula of Pugh [55], a compound exhibits ductile behavior (brittle behavior) if the B_H/G_H ratio is larger

TABLE II. The calculated values of single crystal elastic constants for hexagonal BaPtAs with SrPtSb-type and YPtAs-type crystal structures.

Phase	C_{11} (GPa)	C_{12} (GPa)	C_{13} (GPa)	C_{33} (GPa)	C_{44} (GPa)	C_{66} (GPa)
SrPtSb with SOC	125.03	72.27	36.61	87.43	25.03	26.38
SrPtSb without SOC	129.06	70.73	36.56	88.37	24.55	29.17
YPtAs with SOC	125.24	78.21	37.11	84.87	24.29	23.51
YPtAs without SOC	127.73	78.84	36.70	86.09	24.18	24.45

TABLE III. The calculated values of isotropic bulk modulus B_{VRH}, shear modulus G_{VRH}, Young's modulus E (all in GPa), B_H/G_H ratio, and Poisons's ratio ν for hexagonal BaPtAs with SrPtSb-type and YPtAs-type crystal structures, derived from the values of single-crystal elastic constants.

Phase	B_V	B_R	B_H	G_V	G_R	G_H	E	B_H/G_H	ν
StPtSb with SOC	69.83	64.55	67.19	28.09	27.10	27.59	72.82	2.435	0.319
StPtSb without SOC	70.47	65.06	67.76	29.17	28.05	28.61	75.24	2.368	0.315
YPtAs with SOC	71.13	64.57	67.85	26.61	25.41	26.01	69.19	2.608	0.330
YPtAs without SOC	71.78	65.06	68.42	27.18	25.89	26.54	70.51	2.578	0.328

(smaller) than the critical value of 1.75. As presented in Table III, the corresponding ratio is larger than the critical value for the both phases of BaPtAs, which suggests both phases of BaPtAs to be ductile compounds. Additionally, Cauchy's pressure ($C_p = C_{12} - C_{44}$) is the another physical quantity which describes the ductile/brittle nature of a compound [56]. If this pressure positive (negative), the compound is anticipated to be ductile (brittle). The positive values of this pressure for both phases confirms their ductile nature (see Table II). Furthermore, the value of Poisson's ratio is also used to define compounds with ductility or brittleness. It is proposed that this ratio should be greater (less) then the critical value of 0.26 for ductility (brittleness) [57]. In our case, the calculated values for both phases obviously allude that they are both ductile. The Poisson's ratio also ensures information about the bonding properties of compounds. This ratio takes values around 0.1, 0.25, and 0.33 for covalent, ionic and metallic materials, respectively [57]. As seen from Table III, the value of this ratio for both phases is close to 0.33, indicating that the metallic contribution to the interatomic bonding in both phases is dominant.

It is well know that microcracks are handily caused in solids, which are primarily due to considerable elastic anisotropy. Therefore a suitable parameter to represent the degree of anisotropy is required for single crystals. Several anisotropic indexes are available for defining elastic anisotropy. In our case, the universal anisotropic index (A^U) and percent anisotropy (A_B and A_G) are preferred and estimated by the following equations:

$$A^U = 5\frac{G_V}{G_R} + \frac{B_V}{B_R} - 6 \geqslant 0, \tag{1}$$

$$A_B = \frac{B_V - B_R}{B_V + B_R}, \tag{2}$$

$$A_G = \frac{G_V - G_R}{G_V + G_R}. \tag{3}$$

The calculated values of the above indexes are presented in Table IV. These indexes are weakly effected by the inclusion of SOC. If these indexes equal to zero, it is an isotropic structure; otherwise it is an anisotropic structure. As can be seen from Table IV, the A_G values of both phases are slightly smaller than their A_B values, signaling that they are slightly weak anisotropic in shear modulus. However, the value of A^U is a better indicator for mechanical properties. For both phases, the calculated A_U values are much greater than the calculated A_B and A_G values, implying considerable anisotropic character of them.

The Debye temperature (Θ_D) is a fundamental quantity of a superconductor since it is directly connected to the superconducting transition temperature [45]. This temperature can be derived from the average sound velocity (V_M) in the following equations [58]:

$$\Theta_D = \frac{h}{k_B}\left(\frac{3n}{4\pi}\frac{N_A\rho}{M}\right)^{1/3} V_M, \tag{4}$$

$$V_m = \left[\frac{1}{3}\left(\frac{2}{V_T^3} + \frac{1}{V_L^3}\right)\right]^{-1/3}, \tag{5}$$

$$V_T = \left(\frac{G_H}{\rho}\right)^{1/2}, \tag{6}$$

$$V_L = \left(\frac{3B_H + 4G_H}{3\rho}\right)^{1/2}. \tag{7}$$

Here k_B, h, n, N_A, M, and ρ are the Boltzmann's constant, the Planck's constant, the number of atoms in the molecule, Avogadro's number, the molecular weight, and the density, respectively. V_T and V_L refer to the longitudinal sound velocity and transverse sound velocity, respectively. The calculated values of V_T, V_L, V_M, and Θ_D are summarized in Table IV. This table reveals that the consideration of SOC makes small effect on their values. Especially, the calculated Θ_D values for both phases do not change more than 2% by the inclusion of SOC. Both calculated values of Θ_D, with and without SOC,

TABLE IV. The calculated values of the universal anisotropic index (A^u), percent anisotropy (A_B, A_G), transverse (V_T), longitudinal (V_L), average elastic wave velocities (V_M), and Debye temperature (Θ_D) for hexagonal BaPtAs with SrPtSb-type and YPtAs-type crystal structures.

Phase	A_B	A_G	A^U	V_T (m/s)	V_L (m/s)	V_M(m/s)	Θ_D (K)
SrPtSb with SOC	0.039	0.018	0.264	1808.426	3510.425	2025.002	202
SrPtSb without SOC	0.040	0.019	0.282	1841.309	3542.75	2060.642	205
YPtAs with SOC	0.048	0.023	0.339	1757.444	3489.296	1970.669	196
YPtAs without SOC	0.049	0.024	0.351	1775.281	3510.957	1990.200	198
Experimental [36]							211

TABLE V. The calculated zone-center phonon frequencies (ν in THz), their electron-phonon coupling parameters (λ) and their eigencharacters with SOC for hexagonal BaPtAs with the SrPtSb-type crystal structure. Our results without SOC are presented in brackets. The symbols I and R denote infrared active and Raman active modes, respectively.

Mode	ν	λ	Eigencharacters	Mode	ν	λ	Eigencharacters
A_2'' (I)	2.04 (2.08)	0.06 (0.05)	Ba+Pt+**As**	E' (I+R)	2.28 (2.29)	0.03 (0.02)	**Ba**+Pt+As
A_2'' (I)	3.39 (3.30)	0.01 (0.01)	Ba+Pt+**As**	E' (I+R)	5.64 (5.69)	0.04 (0.04)	Ba+Pt+**As**

for the YPtAs phase are in gratifying accordance with the experimentally measured value [36] of 211 K.

C. Phonons and electron-phonon interaction

The zone center phonon modes of solids must be investigated and discussed in detail since they are play important role in Raman scattering as well as infrared absorption. The zone-center optical phonon modes in the SrPtSb-type BaPtAs can be categorized by the irreducible representations of the point group D_{3h} ($\bar{6}2m$). The group theory foresees the following symmetries of these optical phonon modes:

$$\Gamma(D_{3h}(\bar{6}2m)) = 2A_2'' + 2E',$$

where the A_2'' modes are infrared active and the E' modes are both Raman and infrared active. The A modes arise from the oscillation of relevant atoms along the z axis, while relevant atoms vibrate perpendicular to this axis for the doubly degenerate E modes. The calculated zone-center phonon frequencies, their electron-phonon coupling parameters and the dominant atomic contributions to the eigenvectors of the vibrational phonon modes are presented in Table V. This table also presents the corresponding results without SOC in the brackets. The consideration of SOC causes small amounts of changes in the frequencies of zone-center phonon modes, however it has considerable impact on their electron-phonon coupling parameters. In particular, while the inclusion of SOC decreases the average value of these phonon frequencies ($\overline{\nu}$) from 2.37 to 2.36 THz by less than 1.0%, it increases the average value of their electron-phonon coupling parameters ($\overline{\lambda}$) from 0.020 to 0.023 by around 15%. The values of electron-phonon coupling parameters are mainly influenced by the phonon frequencies and electron-phonon coupling matrix elements. However, the change in $\overline{\nu}$ does not meet the change in $\overline{\lambda}$ due to SOC. Therefore significant changes in the values of electron-phonon coupling parameters can be associated with changes in the electron-phonon coupling matrix elements themselves.

Calculation of electron-phonon coupling requires the understanding of the full phonon spectrum throughout the Brillouin zone. The calculated phonon spectrum of the SrPtSb-type BaPtAs along the high-symmetry directions of hexagonal Brillouin zone is depicted in Fig. 5(a). In general, the phonon spectrum of the SrPtSb-type BaPtAs is similar to that of BaPtSb [35]. A few observations can be made. Low-frequency seven branches are separated from two high-frequency phonon branches by a phonon band gap of 2.06 THz arising from the different mass of the three atomic species. All phonon branches exhibit considerable amount of dispersion expect the two highest optical branches becoming degenerate and flat along the Γ-A symmetry direction. The inclusion of SOC makes a moderate impact on the phonon spectrum of this phase. When this coupling is considered, the frequencies of phonon modes are moderately lowered or moderately increased. The most interesting feature of this phonon spectrum is the hardening of the second transverse acoustic branch close to the M symmetry point. At this symmetry point, with the inclusion of SOC, the frequency of this branch increases from 1.41 to 1.58 THz, by around 12%. This significant hardening lowers the electron-phonon coupling parameter of this phonon modes from 0.65 to 0.45, by slightly less than 31%. The origin of phonon branches in the phonon spectrum can be explained more clearly by examining the total and partial phonon density of states in Fig. 5(b). The hybridized Pt-As vibrations occur at low frequencies below which there is also a sign of strong covalent

TABLE VI. The calculated zone-center phonon frequencies (ν in THz), their electron-phonon coupling parameters (λ) and their eigencharacters with SOC for hexagonal BaPtAs with the YPtAs-type crystal structure. Our results without SOC are presented in brackets. The symbols I, R, and S refer to infrared active, Raman active, and silent modes, respectively.

Mode	ν	λ	Eigencharacters	Mode	ν	λ	Eigencharacters
E_{2g} (R)	0.78 (0.85)	0.01 (0.01)	Ba+**Pt**+As	E_{2u} (S)	0.80 (0.84)	0.00 (0.01)	Ba+**Pt**+As
B_{1g} (S)	1.34 (1.31)	0.03 (0.03)	Ba+**Pt**+As	B_{2u} (S)	1.40 (1.37)	0.02 (0.02)	Ba+**Pt**+As
E_{1g} (R)	1.41 (1.43)	0.01 (0.01)	**Pt**+As	A_{1g} (R)	1.48 (1.50)	0.08 (0.08)	**Pt**+As
A_{2u} (I)	1.71 (1.70)	0.03 (0.02)	Ba+Pt+**As**	E_{1u} (I)	1.73 (1.67)	0.01 (0.01)	**Ba**
B_{1g} (S)	1.77 (1.73)	0.04 (0.05)	Ba+Pt+**As**	B_{2u} (S)	1.93 (1.92)	0.04 (0.04)	Ba+Pt+**As**
E_{2u} (S)	2.06 (2.05)	0.01 (0.00)	**Ba**+Pt+As	E_{2g} (R)	2.20 (2.18)	0.01 (0.01)	**Ba**+Pt+As
E_{1u} (I)	2.32 (2.35)	0.01 (0.01)	**Ba**+Pt+As	A_{2u} (I)	2.50 (2.64)	0.03 (0.04)	**Ba**
A_{1g} (R)	2.86 (2.88)	0.01 (0.01)	Pt+**As**	B_{2u} (S)	3.18 (3.20)	0.02 (0.03)	Ba+Pt+**As**
B_{1g} (S)	3.20 (3.25)	0.02 (0.02)	Ba+Pt+**As**	A_{2u} (I)	3.22 (3.23)	0.00 (0.00)	Ba+Pt+**As**
E_{2u} (S)	5.71 (5.73)	0.01 (0.01)	Ba+Pt+**As**	E_{1u} (I)	5.74 (5.75)	0.01 (0.01)	Pt+**As**
E_{1g} (R)	5.74 (5.75)	0.01 (0.01)	Pt+**As**	E_{2g} (R)	5.76 (5.77)	0.01 (0.02)	Pt+**As**

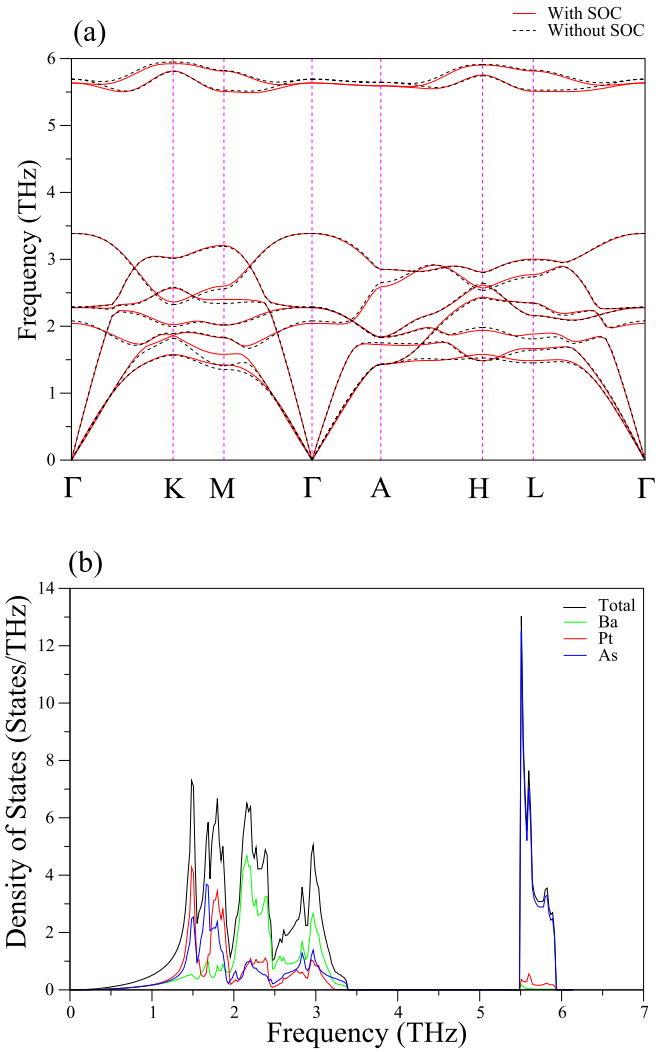

FIG. 5. (a) The calculated phonon spectrum for the SrPtSb-type structure of BaPtAs with and without SOC along the high-symmetry directions in the first Brillouin zone of hexagonal lattice. (b) The calculated total and partial phonon density of states for the SrPtSb-type structure of BaPtAs with SOC included.

interaction between these atoms. The contribution of Ba to phonon modes is strongest in the frequency range from 1.97 to 3.43 THz, while smaller Pt and As contributions are present in this frequency region. Since As is the lightest element, it dominates the high-frequency region above the phonon band gap. We can thus conclude that the low-frequency phonon modes of SrPtSb-type BaPtAs play a crucial role in the transition from the normal state to the superconducting state. The reason for this conclusion is that the electronic bands close the Fermi level are dominated by As p and Pt d states while their hybridized vibrations dominate at low frequencies below 1.97 THz.

Different from the SrPtSb phase, for the YPtAs-type BaPtAs there are 36 phonon branches for each wave vector. According to the group theoretical analysis, the zone-center optical phonon modes of this phase can be decomposed into the irreducible representations of the point group D_{6h} (6/mmm) as follows:

$$\Gamma(D_{6h}(6/mmm)) = 3E_{2g} + 3B_{1g} + 2E_{1g} + 3A_{2u} + 3E_{2u} + 3E_{1u} + 2A_{1g} + 3B_{2u}.$$

The E_{2g}, E_{1g}, and A_{1g} modes are Raman active, while the E_{1u} and A_{2u} modes are infrared active and the rest of them are inactive (silent). The calculated zone-center phonon frequencies, their electron-phonon coupling parameters and the dominant atomic contributions to the eigenvectors of the vibrational phonon modes for this phase are presented in Table VI. This table also presents the corresponding results without SOC in the brackets. Once again, the consideration of SOC causes small amount of changes to the frequencies, but the electron-phonon coupling parameters corresponding to some of the frequencies change by a significant amount. Atomic displacements for the singly degenerate A and B modes are all along the z direction while the doubly degenerate E modes involve the displacement patterns of relevant atoms perpendicular to this direction. The calculated phonon spectrum of the YPtAs-type BaPtAs along the high-symmetry directions of hexagonal Brillouin zone is depicted in Fig. 6(a). All phonon modes have positive frequencies like the SrPtSb phase, certainly implying that BaPtAs is also dynamically stable in its centrosymmetric YPtAs phase. In agreement with the SrPtSb phase, different masses of the three atomic species generate the phonon band gap of 2.13 THz in the phonon spectrum of this phase. This gap separates the phonon spectrum of the YPtAs phase in two regions: one wide region ranging from 0 THz to roughly 3.33 THz and another narrower region from 5.56 to 6.00 THz. These frequency regions contain 28 and 8 branches, respectively. There is significant overlap between the acoustic and low-frequency optical modes in the wider frequency region. Similar to the SrPtSb phase, the inclusion of SOC makes a moderate change on the phonon spectrum of YPtAs-type BaPtAs. The frequencies of phonon modes are increased in some pockets of the zone and decreased in some other pockets of the zone with the inclusion of SOC. The total and partial DOS for the YPtAs-type BaPtAs are displayed in Fig. 6(b). Once again, in the whole of 0–1.92 THz a strong Pt-As hybridization occurs because of a strong covalent interaction between these atoms, while Ba atoms dominate the lattice vibrations between 1.92 and 2.71 THz. Considerable contributions of three atomic species persists in the frequency range from 2.71 to 3.33 THz, while the lightest As atoms dominate the high-frequency region above the phonon band gap.

The essential objective of this theoretical work is to investigate the strength of electron-phonon interaction in the two phases of BaPtAs in order to better find out the origin of superconductivity in them. To that end, we have calculated the Eliashberg spectral function for both phases of BaPtAs. This spectral function allows us to derive the average electron-phonon coupling parameter (λ) and the logarithmically averaged phonon frequency ($\omega_{\ln}$) from its integration by using below equations:

$$\lambda = 2\int_0^\infty \frac{\alpha^2 F(\omega)}{\omega} d\omega \tag{8}$$

and

$$\omega_{\ln} = \exp\left(2\lambda^{-1}\int_0^\infty \frac{d\omega}{\omega}\alpha^2 F(\omega)\ln\omega\right). \tag{9}$$

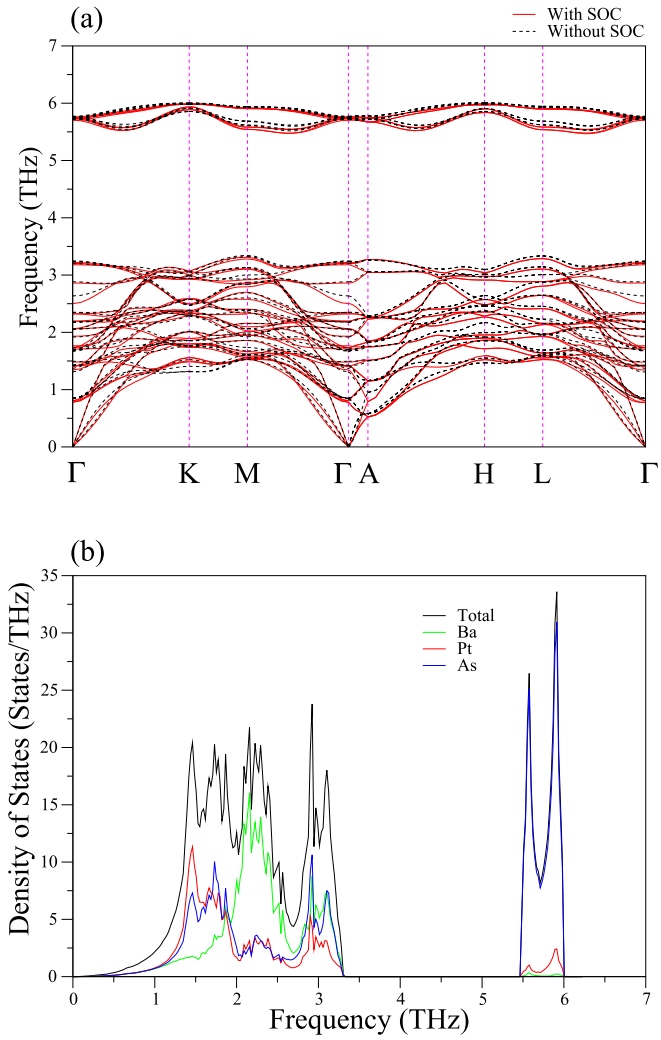

FIG. 6. (a) The calculated phonon spectrum for the YPtAs-type structure of BaPtAs with and without SOC along the high-symmetry directions in the first Brillouin zone of hexagonal lattice. (b) The calculated total and partial phonon density of states for the YPtAs-type structure of BaPtAs with SOC included.

Using the above physical quantities we can obtain the superconducting transition temperature from the Allen-Dynes modified McMillan equations:

$$T_c = \frac{\omega_{\ln}}{1.2}\exp\left(-\frac{1.04(1+\lambda)}{\lambda-\mu^*(1+0.62\lambda)}\right). \qquad (10)$$

Here, μ^* refers to the Coulomb pseudopotential, which determines the strength of the electron-electron interaction. Usually, its value changes between 0.10 and 0.16. In this work, the mean value of 0.13 is preferred for both phases.

The frequency variation of the Eliashberg spectral function $\alpha^2F(\omega)$ and the average electron-phonon coupling parameter λ for the SrPtSb-type BaPtAs are illustrated in Fig. 7. The corresponding results without SOC are shown by dashed lines in this figure. The inclusion of SOC decreases the strength of dominant peaks of the Eliashberg spectral function. Consequently, as can be seen from Fig. 7, this coupling gives rise to the reduction of λ for this phase of BaPtAs. The spectral function $\alpha^2F(\omega)$ shows that lower frequency phonon

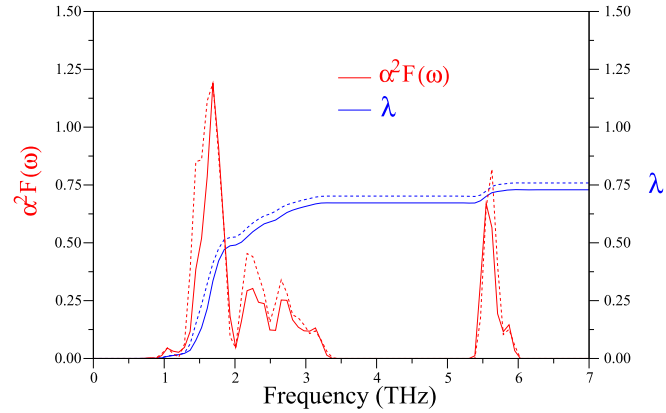

FIG. 7. The frequency variations of the Eliashberg spectral function $\alpha^2F(\omega)$ (red line) and the average electron-phonon coupling parameter λ (blue line) for the SrPtSb-type structure of BaPtAs. Our results without SOC are shown by dashed lines.

modes provide the dominant contribution to electron-phonon coupling. Peculiarly, the vibrations below 1.97 THz offer approximately about 67% to λ. We could expected this result since phonon DOS features in this frequency region arise from the coupled vibrations of Pt and As atoms [see Fig. 5(b)] which dominate electronic states near the Fermi level with their d and p states [see Fig. 2(b)], respectively. Phonon modes in the frequency region between 1.97 and 3.43 THz offer approximately about 25% to λ. This contribution is not surprising since the largest contribution to the DOS features in this frequency region comes from the motion of Ba atom which makes negligible contribution to electronic states close the Fermi level. The phonon modes above the gap region contribute about 8% to λ. This small contribution can be associated with the factor of $1/\omega$ in Eq. (8).

The frequency variation of the Eliashberg spectral function $\alpha^2F(\omega)$ and the average electron-phonon coupling parameter λ for the YPtAs-type BaPtAs are illustrated in Fig. 8. The corresponding results without SOC are shown by dashed lines in this figure. This figure obviously demonstrates that the

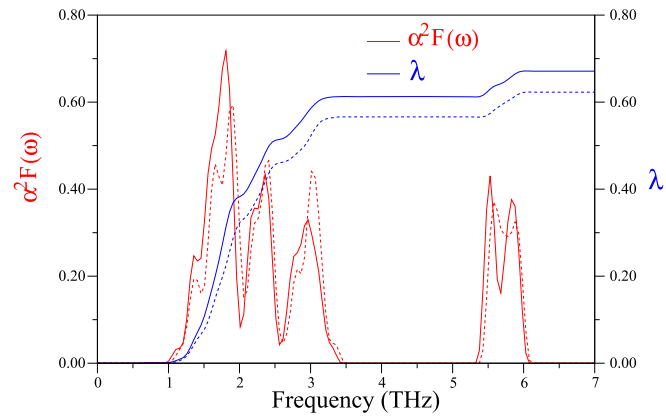

FIG. 8. The frequency variations of the Eliashberg spectral function $\alpha^2F(\omega)$ (red line) and the average electron-phonon coupling parameter λ (blue line) for the YPtAs-type structure of BaPtAs. Our results without SOC are shown by dashed lines.

TABLE VII. The calculated values of physical quantities connected to superconductivity in the hexagonal BaPtAs with SrPtSb-type and YPtAs-type crystal structures. Our results without SOC are presented in brackets. The experimental values of the Debye temperature (Θ_D) and superconducting transition temperature (T_C) are also included for comparison.

Phase	$N(E_F)$ (states/eV per atom)	$\omega_{\ln}$ (K)	λ	Θ_D (K)	T_c (K)
SrPtSb (this work)	0.641 (0.612)	95.98 (92.49)	0.73 (0.78)	203(204)	2.87 (3.25)
SrPtSb (experimental) [36]					2.8
YPtAs (this work)	0.627 (0.603)	101.27 (105.95)	0.67 (0.62)	207 (206)	2.38 (1.95)
YPtAs (experimental) [36]				211	2.1-3.0

inclusion of SOC gives rise to an opposite effect on the electron-phonon interaction properties of YPtAs-type BaPtAs as compared to its SrPtSb-type phase. This coupling leads to increase the strength of dominant peaks of the Eliashberg spectral function and thus it increases the value of λ for the YPtAs-type BaPtAs. Once again, the hybridized Pt-As vibrations play a strongly significant role in determining the electron-phonon interaction properties of this phase since phonon modes below around 1.92 THz contribute about 56% to λ. On the other hand, phonon modes between 1.92 and 3.33 THz make contribution about 36% to λ while phonon modes above the gap region contribute about 8% to λ. Clearly, the analysis of $\alpha^2F(\omega)$ for both phases reveals that the phonon modes with lower frequency (below around 2.0 THz) are more involved in the process of scattering of electrons than the phonon modes with higher frequency.

The calculated values of the physical quantities [$N(E_F)$, $\omega_{\ln}$, λ, Θ_D, and T_c] with and without SOC associated with superconductivity in the both phases of BaPtAs are summarized in Table VII. Note that the values of Θ_D are calculated within the quasi-static harmonic approximation [59,60]. For the SrPtSb phase, the inclusion of SOC diminishes the value of λ from 0.78 to 0.73 K, by around 6%. This reduction of λ arising from the inclusion of SOC decreases the value of T_c from 3.25 to 2.87 K. The latter value of T_c is in excellent agreement with the recent measured value [36] of 2.8 K. As can be seen from Table VII, the scenario is opposite for the YPtAs phase of BaPtAs. When SOC is taken into account, the value of λ increases from 0.62 to 0.67, by around 7%, which gives rise to the increase of T_c from 1.95 to 2.38 K. Although the SrPtSb phase of BaPtAs does not contain a center of inversion different from its YPtAs phase, the inclusion of SOC almost makes a similar level of effect on the electron-phonon interaction properties of both phases. Eventually, the conventional electron-phonon coupling picture readily explains the existence of superconductivity in the both phases of BaPtAs.

Now, we are going to make a comparison, as regards superconductivity, between the SrPtSb-type BaPtAs and its isostructural and isoelectronic compound BaPtSb [35] by examining their electronic, phonon and electron-phonon interaction properties. This comparison is realized in Table VIII. As can be seen from this table, the inclusion of SOC makes the same level of effect on the electronic properties for both centrosymmetric superconductors because their $N(E_F)$ values are slightly increased by the inclusion of this coupling. However, the situation is opposite for their $\omega_{\ln}$ values. When SOC is considered, the value of $\omega_{\ln}$ for BaPtSb is decreased from 82.21 to 80.93 K. Since the soft mode is favorable to superconductivity, this softening increases the value of λ from 0.62 to 0.63. Therefore the inclusion of this coupling increases the T_c value of BaPtSb from 1.46 to 1.54 K. However, Table VIII obviously reveals the opposite scenario for the SrPtSb-type BaPtAs. This difference can be related to phonon properties of these superconductors due to the considerable mass difference between Sb and As atoms since both superconductors are isostructural and isoelectronic to each other.

IV. SUMMARY

Recently, the intermetallic compound BaPtAs has been reported to adopt the hexagonal noncentrosymmetric SrPtSb-type crystal structure as well as hexagonal centrosymmetric YPtAs-type crystal structure. These phases of BaPtAs provide a perfect platform for searching the effect of spin-orbit coupling on superconductivity with broken and preserved spatial inversion symmetries. This reality has led us to examine the effect of spin-orbit coupling on the physical and electron-phonon interaction properties by using the generalized gradient approximation of the density functional theory and the plane-wave pseudopotential method.

It is found that in the noncentrosymmetric SrPtSb-type crystal structure (i) SOC lifts degeneracies of electronic bands at the H symmetry point and (ii) the lack of inversion symmetry results in an antisymmetric spin-orbit coupling which removes twofold degeneracy of electronic bands in the Γ-K, A-H, H-L, and Γ-L symmetry directions. In the case of YPtAs-type BaPtAs, effect (ii) is absent since the YPtAs-type crystal structure contains a center of inversion. In general, effect (i) on the electronic bands close to the Fermi level remains small as for the other crystal phase. The value of

TABLE VIII. Comparison of superconducting state parameters for BaPtAs and BaPtSb with the SrPtSb-type crystal structure. Our results without SOC are presented in brackets.

Compound	$N(E_F)$ (states/eV per atom)	$\omega_{\ln}$(K)	λ	T_c(K)
BaPtAs	0.641 (0.612)	95.98 (92.49)	0.73 (0.78)	2.87 (3.25)
BaPtSb [35]	0.620 (0.600)	80.93 (82.21)	0.63 (0.62)	1.54 (1.46)

density of states at the Fermi level for both phases does not change more than 5% with the inclusion of SOC. For both phases, Pt 5*d* and As 4*p* orbitals play the main role in the formation of the superconducting state since they dominate the electronic states close to the Fermi level.

An analysis of electronic results for both phases of BaPtAs reveals the combinations of ionic, covalent and metallic bonds in their bonding. Single-crystal elastic constants, obtained using the stress-strain method based on the generalized Hooke's law, hint that both phases of BaPtAs are mechanically stable in their crystal structures based on well accordance with elastic criteria of hexagonal systems. For both phases, the inclusion of spin-orbit coupling does not make any significant effect on the values of elastic constants and elastic moduli. The ratio of bulk modulus to shear modulus and the value of Poisson's ratio for both phases indicate that they behave in a ductile manner.

The consideration of SOC has a moderate impact on the phonon dispersion relations in both phases of BaPtAs: the frequencies of some phonon modes are moderately lowered or moderately increased. Hybridized Pt-As vibrations occur at low frequencies (below around 2.0 THz) due to a strong covalent interaction between these atoms. Therefore the low-frequency phonon modes due to the coupled vibrations of Pt and As atoms play an essential role in the transition from the normal state to the superconducting states since Pt *d* and As *p* states dominate electronic sates near the Fermi level.

In general, the inclusion of SOC does not have strong effect on the electron-phonon interaction properties, as there is only moderate effect of this coupling on the electronic band structures and the phonon band structures. However, this coupling makes an opposite impact on the Eliashberg spectral function for the two phases of BaPtAs. For the non-centrosymmetric phase, this coupling decreases the strength of dominant peaks of its Eliashberg spectral function, and hence reduces the values of average electron-phonon coupling and superconducting transition temperature. On the other hand, the scenario is exactly opposite for the centrosymmetric phase. For both phases, the hybridized Pt-As vibrations play a strongly significant role in determining their electron-phonon interaction properties since they make a largest contribution to the value of average electron-phonon coupling parameter. Finally, using the Allen-Dynes modified McMillian equation with the screened Coulomb pseudopotential parameter $\mu^* = 0.13$, the superconducting temperature of BaPtAs is estimated to be 2.87 K for the SrPtSb phase and 2.38 K for the YPtAs phase. These values compare very well with the reported measured values of 2.8 K and 2.1–3.0 K. We thus conclude that the conventional electron-phonon coupling picture is able to explain the origin of superconductivity in both phases of hexagonal BaPtAs.

[1] L. P. Gor'kov and E. I. Rashba, Superconducting 2D System with Lifted Spin Degeneracy: Mixed Singlet-Triplet State, Phys. Rev. Lett. **87**, 037004 (2001).

[2] E. Bauer, G. Hilscher, H. Michor, Ch. Paul, E. W. Scheidt, A. Gribanov, Yu. Seropegin, H. Noêl, M. Sigrist, and P. Rogl, Heavy Fermion Superconductivity and Magnetic Order in Noncentrosymmetric $CePt_3Si$, Phys. Rev. Lett. **92**, 027003 (2004).

[3] N. Kimura, K. Ito, K. Saitoh, Y. Umeda, H. Aoki, and T. Terashima, Pressure-Induced Superconductivity in Noncentrosymmetric Heavy-Fermion $CeRhSi_3$, Phys. Rev. Lett. **95**, 247004 (2005).

[4] N. Tateiwa, Y. Haga, T. D. Matsuda, S. Ikeda, E. Yamamoto, Y. Okuda, Y. Miyauchi, R. Settai, and Y. Onuki, Strong-coupling superconductivity of $CeIrSi_3$ with the non-centrosymmetric crystal structure, J. Phys. Soc. Jpn. **76**, 083706 (2007).

[5] R. Settai, Y. Okuda, I. Sugitani, Y. Ōnuki, T. D. Matsuda, Y. Haga, and H. Harima, Non-centrosymmetric heavy fermion superconductivity in $CeCoGe_3$, Int. J. Mod. Phys. B **21**, 3238 (2007).

[6] M. Sigrist, D. Agterberg, P. Frigeri, N. Hayashi, R. Kaur, A. Koga, I. Milat, and K. W. Y. Yanase, Superconductivity in non-centrosymmetric materials, J. Magn. Magn. Mater. **310**, 536 (2007).

[7] E. Bauer and M. Sigrist, *Noncentrosymmetric Superconductors: Introduction and Overview* (Springer Verlag, Berlin, Heidelberg, 2012).

[8] S. Yip, Noncentrosymmetric superconductors, Annu. Rev. Condens. Mater. Phys. **5**, 15 (2014).

[9] F. Kneidinger, E. Bauer, I. Zeiringer, P. Rogl, C. Blass-Schenner, D. Reith, and R. Podloucky, Superconductivity in non-centrosymmetric materials, Physica C **514**, 388 (2015).

[10] M. Smidman, M. B. Salamon, H. Q. Yuan, and D. F. Agterberg, Superconductivity and spin-orbit coupling in noncentrosymmetric materials: A review, Rep. Prog. Phys. **80**, 036501 (2017).

[11] K. Togano, P. Badica, Y. Nakamori, S. Orimo, H. Takeya, and K. Hirata, Superconductivity in the Metal Rich Li-Pd-B Ternary Boride, Phys. Rev. Lett. **93**, 247004 (2004).

[12] P. Badica, T. Kondo, and K. Togano, Superconductivity in a new pseudo-binary $Li_2B(Pd_{1-x}Pt_x)_3$ (x=0−1) boride system, J. Phys. Soc. Jpn. **74**, 1014 (2005).

[13] H. Takeya, K. Hirata, K. Yamaura, and K. T. M. El Massalami, R. Rapp, F. A. Chaves, and B. Ouladdiaf, Low-temperature specific-heat and neutron-diffraction studies on Li_2Pd_3B and Li_2Pt_3B superconductors, Phys. Rev. B **72**, 104506 (2005).

[14] A. D. Hillier, J. Quintanill, and R. Cywinski, Evidence for Time-Reversal Symmetry Breaking in the Noncentrosymmetric Superconductor $LaNiC_2$, Phys. Rev. Lett. **102**, 117007 (2009).

[15] L. Fang, H. Yang, X. Zhu, G. Mu, Z.-S. Wang, L. Shan, C. Ren, and H.-H. Wen, Physical properties of the noncentrosymmetric superconductor Ru_7B_3, Phys. Rev. B **79**, 144509 (2009).

[16] E. Bauer, R. T. Khan, H. Michor, E. Royanian, A. Grytsiv, N. Melnychenko-Koblyuk, P. Rogl, D. Reith, R. Podloucky, E.-W. Scheidt, W. Wolf, and M. Marsman, $BaPtSi_3$: A non-centrosymmetric BCS-like superconductor, Phys. Rev. B **80**, 064504 (2009).

[17] V. K. Anand, A. D. Hillier, D. T. Adroja, A. M. Strydom, H. Michor, K. A. McEwen, and B. D. Rainford, Specific heat and lSR study on the noncentrosymmetric superconductor $LaRhSi_3$, Phys. Rev. B **83**, 064522 (2011).

[18] G. Eguchi, D. C. Peets, M. Kriener, Y. Maeno, E. Nishibori, Y. Kumazawa, K. Banno, S. Maki, and H. Sawa, Crystallographic and superconducting properties of the fully gapped noncentrosymmetric 5d-electron superconductors $CaMSi_3$(M = Ir, Pt), Phys. Rev. B **83**, 024512 (2011).

[19] M. Smidman, A. D. Hillier, D. T. Adroja, M. R. Lees, V. K. Anand, R. P. Singh, R. I. Smith, D. M. Paul, and G. Balakrishnan, Investigations of the superconducting states of noncentrosymmetric $LaPdSi_3$ and $LaPtSi_3$, Phys. Rev. B **89**, 094509 (2014).

[20] V. K. Anand, D. Britz, A. Bhattacharyya, D. T. Adroja, A. D. Hillier, A. M. Strydom, W. Kockelmann, B. D. Rainford, and K. A. McEwen, Physical properties of noncentrosymmetric superconductor $LaIrSi_3$: A μSR study, Phys. Rev. B **90**, 014513 (2014).

[21] M. Isobe, M. Arai, and N. Shirakawa, Superconductivity in noncentrosymmetric $SrAuSi_3$, Phys. Rev. B **93**, 054519 (2016).

[22] A. B. Karki, Y. M. Xiong, I. Vekhter, D. Browne, P. W. Adams, and D. P. Young, K. R. Thomas and J. Y. Chan, H. Kim, and R. Prozorov, Structure and physical properties of the noncentrosymmetric superconductor Mo_3Al_2C, Phys. Rev. B **82**, 064512 (2010).

[23] R. P. Singh, A. D. Hillier, B. Mazidian, J. Quintanilla, J. F. Annett, D. McK. Paul, G. Balakrishnan, and M. R. Lees, Detection of Time-Reversal Symmetry Breaking in the Noncentrosymmetric Superconductor Re_6Zr Using Muon-Spin Spectroscopy, Phys. Rev. Lett. **112**, 107002 (2014).

[24] W. Wei, G. J. Zhao, D. R. Kim, C. Jin, J. L. Zhang, L. Ling, L. Zhang, H. Du, T. Y. Chen, J. Zang, M. Tian, C. L. Chien, and Y. Zhang, Rh_2Mo_3N : Noncentrosymmetric s -wave superconductor, Phys. Rev. B **94**, 104503 (2016).

[25] K. Kudo, Y. Saito, T. Takeuchi, Shin-ya Ayukawa, T. Kawamata, S. Nakamura, Y. Koike, and M. Nohara, Superconductivity in BaPtSb with an ordered honeycomb network, J. Phys. Soc. Jpn. **87**, 063702 (2018).

[26] K.-W. Lee and W. E. Pickett, Crystal symmetry, electron-phonon coupling, and superconducting tendencies in Li_2Pd_3B and Li_2Pt_3B, Phys. Rev. B **72**, 174505 (2005).

[27] B. Wiendlocha, R. Szczesniak, A. P. Durajski, and M. Muras, Pressure effects on the unconventional superconductivity of noncentrosymmetric $LaNiC_2$, Phys. Rev. B **94**, 134517 (2016).

[28] V. V. Bannikov, I. R. Shein, and A. L. Ivanovskii, Structural and electronic properties and the fermi surface of the new noncentrosymmetric superconductors: 3.6 K $CaIrSi_3$ and 2.3 K $CaPtSi_3$, JETP Lett. **92**, 343 (2010).

[29] J. Kaczkowski and A. Jezierski, First-principle study on electronic and structural properties of newly discovered superconductors: $CaIrSi_3$ and $CaPtSi_3$, J. Alloys Compd. **509**, 6142 (2011).

[30] M. J. Winiarski and M. Samsel-Czekala, Electronic structure of noncentrosymmetric superconductor $LaPdSi_3$ and its reference compound $LaPdGe_3$, Intermetallics **56**, 44 (2015).

[31] E. Arslan, E. Karaca, Tütüncü, A. Basoglu, and G. P. Srivastava, Theoretical investigation of superconductivity in $SrAuSi_3$ and $SrAu_2Si_2$, J. Phys. Chem. Solids **95**, 65 (2016).

[32] H. Y. Uzunok, E. Ipsara, H. M. Tütüncü, G. P. Srivastava, and A. Basoglu, The effect of spin orbit interaction for superconductivity in the noncentrosymmetric superconductor $CaIrSi_3$, J. Alloys Compd. **681**, 205 (2016).

[33] H. Y. Uzunok, H. M. Tütüncü, G. P. Srivastava, and A. Basoglu, The influence of spin orbit interaction on phonons and superconductivity in the noncentrosymmetric superconductors $LaPt_3Si$ and $LaPtSi_3$, Intermetallics **86**, 1 (2017).

[34] H. Y. Uzunok, H. M. Tütüncü, G. P. Srivastava, E. Ipsara, and A. Basoglu, The effect of spin orbit interaction on the physical properties of $LaTSi_3$ (T = Ir, Pd, and Rh): First-principles calculations, J. Appl. Phys. **121**, 193904 (2017).

[35] H. Y. Uzunok, H. M. Tütüncü, E. Karaca, and G. P. Srivastava, Theoretical investigation of antisymmetric spin-orbit coupling effect on the physical properties of noncentrosymmetric BaPtSb superconductor, Intermetallic **108**, 109 (2019).

[36] K. Kudo, T. Takeuchi, H. Ota, Y. Saito, S.-y. Ayukawa, K. Fujimura, and M. Nohara, Superconductivity in hexagonal baptas: SrPtSb-and YPtAs-type structures with ordered honeycomb network, J. Phys. Soc. Jpn. **87**, 073708 (2018).

[37] P. Giannozzi, S. Baroni, N. Bonini, M. Calandra, R. Car, C. Cavazzoni, D. Ceresoli, G. L. Chiarotti, M. Cococcioni, I. Dabo, A. Dal Corso, S. de Gironcoli, S. Fabris, G. Fratesi, R. Gebauer, U. Gerstmann, C. Gougoussis, A. Kokalj, M. Lazzeri, L. Martin-Samos, N. Marzari, F. Mauri, R. Mazzarello, S. Paolini, A. Pasquarello, L. Paulatto, C. Sbraccia, S. Scandolo, G. Sclauzero, A. P. Seitsonen, A. Smogunov, P. Umari, and R. M. Wentzcovitch, QUANTUM ESPRESSO: A modular and open-source software project for quantum simulations of materials, J. Phys.: Condens. Matter **21**, 395502 (2009).

[38] P. Giannozzi, O. Andreussi, T. Brumme, O. Bunau, M. Buongiorno Nardelli, M. Calandra, R. Car, C. Cavazzoni, D. Ceresoli, M. Cococcioni, N. Colonna, I. Carnimeo, A. Dal Corso, S. de Gironcoli, P. Delugas, R. A. DiStasio, Jr., A. Ferretti, A. Floris, G. Fratesi, G. Fugallo, R. Gebauer, U. Gerstmann, F. Giustino, T. Gorni, J. Jia, M. Kawamura, H.-Y. Ko, A. Kokalj, E. Küçükbenli, M. Lazzeri, M. Marsili, N. Marzari, F. Mauri, N. L. Nguyen, H.-V. Nguyen, A. Otero-de-la-Roza, L. Paulatto, S. Poncé, D. Rocca, R. Sabatini, B. Santra, M. Schlipf, A. P. Seitsonen, A. Smogunov, I. Timrov, T. Thonhauser, P. Umari, N. Vast, X. Wu, and S. Baroni, Advanced capabilities for materials modeling with Quantum ESPRESSO, J. Phys.: Condens. Matter **29**, 465901 (2017).

[39] L. Farst, J. M. Wills, B. Johansson, and E. Erikson, Elastic constants of hexagonal transtion metal, Phys. Rev. B **51**, 17431 (1995).

[40] W. Voigt, *Lehrbuch der Kristallphysik: mit Ausschluß der Kristalloptik* (Leipzig-Vieweg+Teubner Verlag, 1966).

[41] A. Reuss, Berechnung der fließgrenze von mischkristallen auf grund der plastizitätsbedingung für einkristalle, Z. Angew. Math. Mech. **9**, 49 (1929).

[42] R. Hill, The elastic behavior of a crystalline aggregate, Proc. Phys. Soc. Sect. A **65**, 349 (1952).

[43] A. B. Migdal, Interaction between electrons and lattice vibrations in a normal metal, Zh. Eksp. Teor. Fiz. **34**, 1438 (1958) [JETP **34**, 996 (1958)].

[44] G. M. Eliashberg, Interaction between electrons and lattice vibrations in a superconductor, Zh. Eksp. Teor. Fiz. **38**, 966 (1960) [JETP **11**, 696 (1960)].

[45] P. B. Allen and R. C. Dynes, Transition temperature of strong-coupled superconductors reanalyzed, Phys. Rev. B **12**, 905 (1975).

[46] A. M. Rappe, K. M. Rabe, E. Kaxiras, and J. D. Joannopoulos, Optimized pseudopotentials, Phys. Rev. B **41**, 1227 (1990).

[47] J. P. Perdew, K. Burke, and M. Ernzerhof, Generalized Gradient Approximation Made Simple, Phys. Rev. Lett. **77**, 3865 (1996).

[48] T. H. Fischer and J. Almlof, General methods for geometry and wave function optimization, J. Phys. Chem. **96**, 9768 (1992).

[49] W. Kohn and L. J. Sham, Self-consistent equations including exchange and correlation effects, Phys. Rev. **140**, A1133 (1965).

[50] H. J. Monkhorst and J. D. Pack, Special points for Brillouin-zone integrations, Phys. Rev. B **13**, 5188 (1976).

[51] H. M. Tütüncü, H. Y. Uzunok, E. Karaca, G. P. Srivastava, S. Özer, and Ş. Uğur, *Ab initio* investigation of BCS-type superconductivity in $LuNi_2B_2C$-type superconductors, Phys. Rev. B **92**, 054510 (2015).

[52] F. D. Murnaghan, The compressibility of media under extreme pressures, Proc. Natl. Acad. Sci. USA **30**, 244 (1944).

[53] H. Q. Yuan, D. F. Agterberg, N. Hayashi, P. Badica, D. Vandervelde, K. Togano, M. Sigrist, and M. B. Salamon, S-Wave Spin-Triplet Order in Superconductors without Inversion Symmetry:Li_2Pd_3B and Li_2Pt_3B, Phys. Rev. Lett. **97**, 017006 (2006).

[54] T. Takimoto and P. Thalmeier, Triplet cooper pair formation by anomalous spin fluctuations in non-centrosymmetric superconductors, J. Phys. Soc. Jpn. **78**, 103703 (2009).

[55] S. F. Pugh, XCII. Relations between the elastic moduli and the plastic properties of polycrystalline pure metals, Philos. Mag. **45**, 823 (1954).

[56] S. Ganeshan, S. L. Shang, H. Zhang, Y. Wang, M. Mantina, and Z. K. Liu, Elastic constants of binary Mg compounds from first-principles calculations, Intermetallics **17**, 313 (2009).

[57] J. Haines, J. M. Leger, and G. Bocquillon, Synthesis and design of superhard materials, Annu. Rev. Mater. Res. **31**, 1 (2001).

[58] O. L. Anderson, A simplified method for calculating the Debye temperature from elastic constants, J. Phys. Chem. Solids **24**, 909 (1963).

[59] S. Baroni, P. Giannozzi, and E. Isaev, Theoretical and computational methods in mineral physics: Geophysical applications, Mineral. Geochem. **71**, 39 (2010).

[60] Y. Wang, J. J. Wang, H. Zhang, V. R. Manga, S. L. Shang, L.-Q. Chen, and Z.-K. Liu, A first-principles approach to finite temperature elastic constants, J. Phys.: Condens. Matter **22**, 225404 (2010).